A Hot Cusp-shaped Confined Solar Flare

Aaron Hernandez-Perez[1] , Yang Su[2] , Julia Thalmann[1] , Astrid M. Veronig[1] , Ewan C. Dickson[1], Karin Dissauer[1] ,
Bhuwan Joshi[3] , and Ramesh Chandra[4]

[1] University of Graz, Institute of Physics/IGAM, A-8010 Graz, Austria; aaron.hernandez-perez@uni-graz.at
[2] Key Laboratory of Dark Matter and Space Astronomy, Purple Mountain Observatory Chinese Academy of Sciences, 10 Yuanhua Road, Nanjing 210033, People's Republic of China; yang.su@pmo.ac.cn
[3] Udaipur Solar Observatory, Physical Research Laboratory, Udaipur 313 001, India
[4] Department of Physics, DSB Campus, Kumaun University, Nainital 263 002, India
Received 2019 September 6; revised 2019 November 19; accepted 2019 November 25; published 2019 December 17

Abstract

We analyze a confined flare that developed a hot cusp-like structure high in the corona ($H \sim 66$ Mm). A growing cusp-shaped flare arcade is a typical feature in the standard model of eruptive flares, caused by magnetic reconnection at progressively larger coronal heights. In contrast, we observe a static hot cusp during a confined flare. Despite an initial vertical temperature distribution similar to that in eruptive flares, we observe a distinctly different evolution during the late (decay) phase, in the form of prolonged hot emission. The distinct cusp shape, rooted at locations of nonthermal precursor activity, was likely caused by a magnetic field arcade that kinked near the top. Our observations indicate that the prolonged heating was a result of slow local reconnection and an increased thermal pressure near the kinked apexes due to continuous plasma upflows.

Unified Astronomy Thesaurus concepts: Solar corona (1483); Solar flares (1496); Solar X-ray emission (1536); Solar ultraviolet emission (1533)

Supporting material: animations

1. Introduction

Solar flares are explosive events in which magnetic energy is rapidly converted into plasma heating and particle acceleration (e.g., Benz 2017). The most accepted model for eruptive flares is the so-called CSHKP model (e.g., Carmichael 1964; Sturrock 1966; Hirayama 1974; Kopp & Pneuman 1976). In the simplistic view of this 2D framework, an erupting flux rope stretches the magnetic field underneath, forming a current sheet, toward which the embedding field is drawn and forced to reconnect (Forbes 2000). The ability to explain many features observed in eruptive flares is where the success of this model resides. For instance, hot cusp-shaped coronal structures often observed in flares are regarded as observational evidence of the reconnection process (Tsuneta et al. 1992). These structures exhibit an increasing temperature with altitude, caused by the newly reconnected fields, which are drawn back from the reconnection site (Tsuneta 1996). As reconnection occurs progressively higher up in the corona, the flare arcade grows, accompanied by a separation in the quasi-parallel ribbons, establishing the connectivity between the newly reconnected loops and the chromosphere (e.g.,Veronig et al. 2006).

Despite the ability of the CSHKP model to describe several features in eruptive flares, a significant fraction of the flares are confined (i.e., they are not associated with the eruption of a flux rope). Confined flares cannot be accommodated in the standard flare model, and other theories are needed to understand their physics. Several models have been proposed including, e.g., quadrupolar current-loop interaction (e.g., Melrose 1997), emerging flux (Heyvaerts et al. 1977), or the fan-spine topology (e.g., Masson et al. 2009). These models can explain features of confined flares that deviate from those observed of eruptive flares, e.g., the interaction between current-carrying loops (e.g., Yurchyshyn et al. 2000; Glesener et al. 2017), the interaction of emerging flux and coronal fields (e.g., Veronig & Polanec 2015), and the formation of circular

or quasi-circular ribbons (e.g., Reid et al. 2012; Joshi et al. 2015; Hernandez-Perez et al. 2017; Li et al. 2018b; Chen et al. 2019; Hou et al. 2019; Zhang et al. 2019; Zhong et al. 2019).

However, although rarely reported in literature, some confined flares occasionally exhibit features similar to those observed in eruptive flares. For instance, observational evidence of cusp-shaped loops have been reported on two occasions. Liu et al. (2014) reported a confined flare exhibiting a diffusive cusp-shaped structure, which was interpreted as a result of the sudden changes in the magnetic field connectivity that reconnected across a quasi-separatrix layer. However, unlike in eruptive flares, the temperature in the cusp was lower than the underlying flare arcade. Gou et al. (2015) presented observations of a confined event (event No. 6 in their sample) that exhibited a double candle-flame configuration, i.e., two cusp-shaped structures located side by side, that shared the cusp-shaped edges. They observed a temperature distribution that was similar to those typically observed in eruptive events, and interpreted this phenomenon as heating from the slow-mode shocks from the reconnection site.

We report an atypical confined flare (SOL2014-01-13T21:51M1.3) that exhibited an apparent cusp with a temperature distribution otherwise usually only observed for eruptive flares. The decay phase was characterized by unusual prolonged hot emission, originating from the cusp's apex. This study presents a new scenario in the initiation of confined cusp-shaped flares and aims to elucidate the mechanism responsible for the extended heating.

2. Data and Methods

We used (extreme) ultraviolet ((E)UV) data from the Atmospheric Imaging Assembly (AIA; Lemen et al. 2012) on board the *Solar Dynamics Observatory* (*SDO*; Pesnell et al. 2012) to study the evolution of the flare plasma. To study the nonthermal signatures of accelerated electrons as well as the
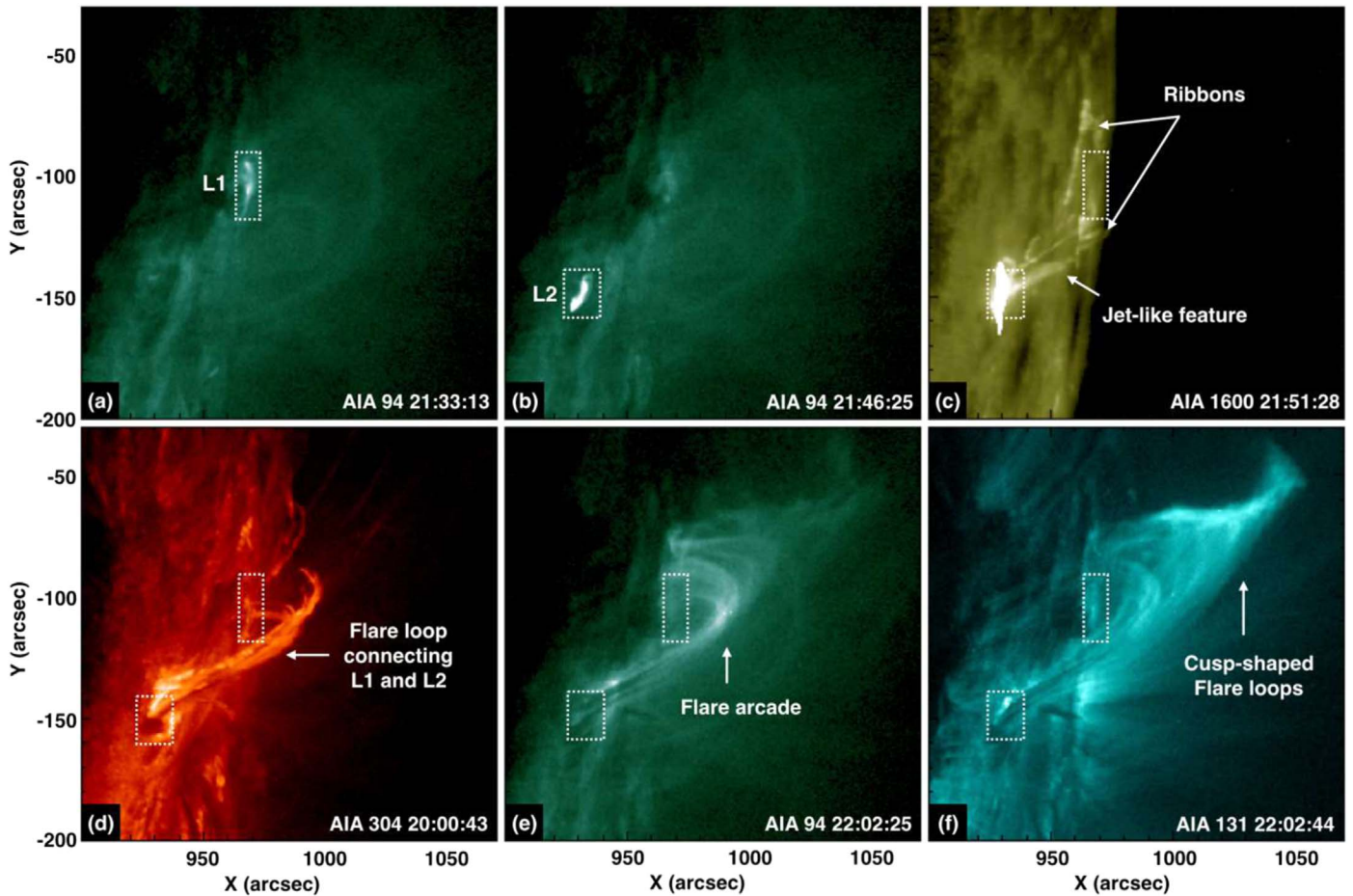
Figure 1. (E)UV sequence showing the main aspects of SOL2014-01-13T21:51M1.3 in different AIA filters. (a), (b) EUV precursor brightenings at L1 and L2. (c) Formation of ribbons and jet-like feature during the impulsive phase. (d)–(f) EUV sequence of the decay phase, showing the connectivity between the precursor sites and the cusp-shaped flare loops. The animation shows the evolution of the flare in co-temporal AIA 1600, 304, 94, and 131 Å maps. An animation of the four AIA filters is available. The video begins at after 21:30 and ends before 22:15. The realtime duration of the animation is 15 s.

(An animation of this figure is available.)

hot thermal flare emission, we used hard X-ray data from the *Ramaty High Energy Spectroscopic Imager* (*RHESSI*; Lin et al. 2002) and the *FERMI* satellite (Meegan et al. 2009). *RHESSI* CLEAN images (Hurford et al. 2002) were constructed using the front segments of detectors 1, 3, 4, 5, 6, 8, and 9. X-ray spectra were fitted with an isothermal model and, when appropriate, a thick-target nonthermal emission model (Brown 1971; Holman et al. 2003). For the spectral analysis, we selected the detectors that provided the best fitting results, namely 4 and 6 for *RHESSI*. For *FERMI*/GBM, detector 5 was used, as it was pointing to the Sun during the flare.

The thermal evolution of the flare plasma was studied by means of a Differential Emission Measure (DEM) analysis on AIA EUV filtergrams. We used the Sparse inversion method developed by Cheung et al. (2015), with the new settings proposed by Su et al. (2018).

3. Results

3.1. Event Overview

The confined M1.3–class flare on 2014 January 13 occurred in NOAA AR 11944 near the western solar limb (S10W81). Figures 1 and animation 1 show the main (E)UV aspects of SOL2014-01-13T21:51M1.3. The early phase was characterized by localized (E)UV enhancements (i.e., precursors) at two locations very low in the corona (marked as L1 and L2 in Figures 1(a), (b)), separated by a projected distance of ~37 Mm. The triggering of the flare produced a jet-like feature and ribbons encompassing L1 (Figure 1(c)). The direct connectivity between the precursor sites was observed by hot flare loops connecting L1 and L2 during the flare decay phase (Figure 1(d)). The EUV emission during the decay phase revealed the flare arcade, and the hot cusp-shaped flare loops (Figures 1(e), (f)), extending up to ~66 Mm above the solar surface (distance measured from L1 to the highest point). Prolonged hot emission of the cusp-shaped flare loops followed (see animation 1).

In order to understand the formation of this unusual coronal structure and its subsequent prolonged hot emission, we need to understand the chain of events that led to the flare and its underlying magnetic configuration. The following sections present a detailed description and analysis of the flare characteristics, chronologically addressing (1) the flare precursors, (2) the causal relationship between precursors and flare features, and (3) the characteristics of the cusp-shaped flare loops and the prolonged hot emission.
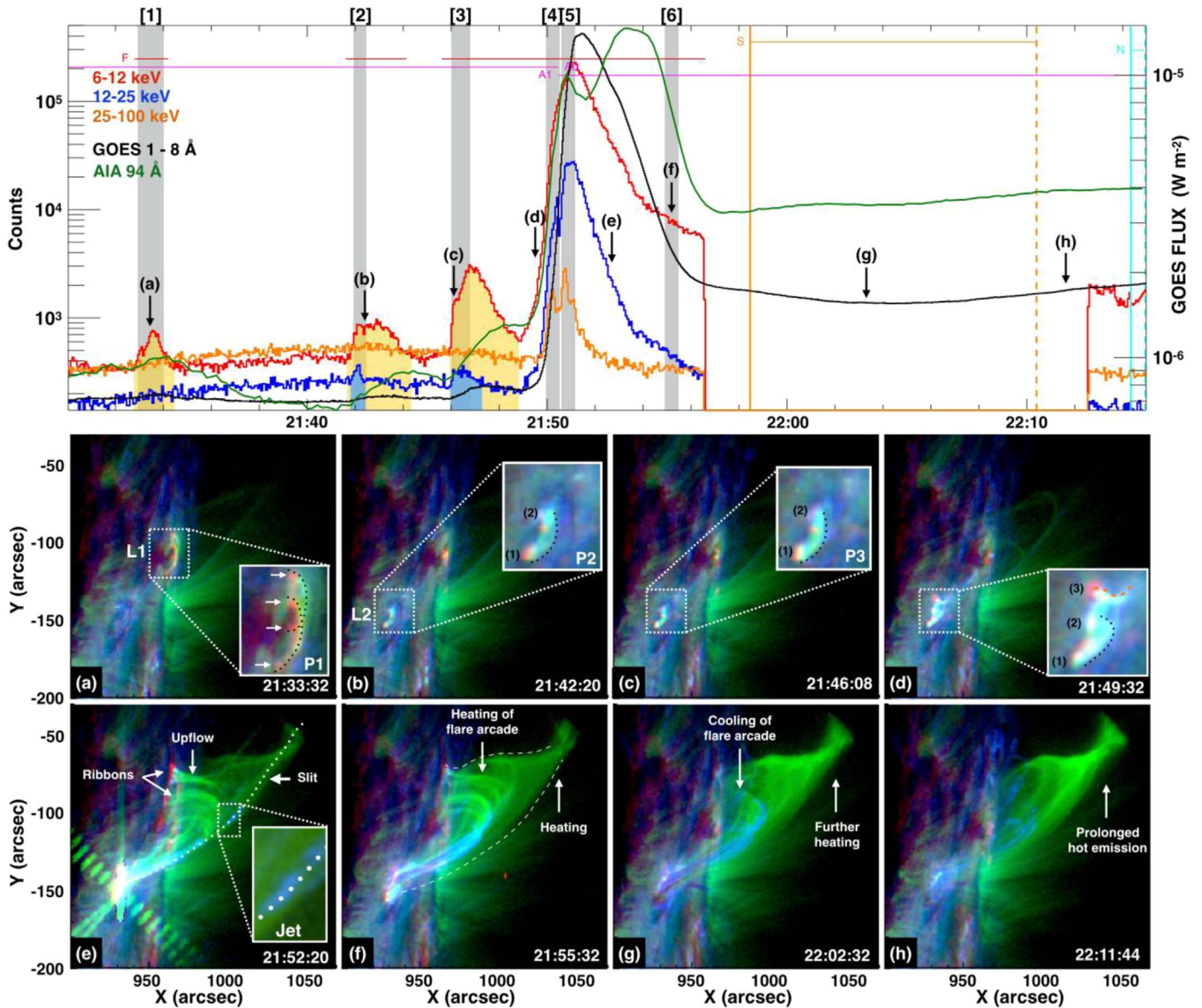
Figure 2. Top: *RHESSI* X-ray counts, for the 6–12 (red), 12–25 (blue), and 25–100 keV (orange) energy bands, *GOES* SXR flux in the 1–8 Å wavelength band (black solid line), and normalized AIA 94 Å lightcurve for the field of view (FOV) in the bottom panels (green solid line). The yellow and blue areas highlight the enhanced X-ray precursor emission in the 6–12 and 12–25 keV energy bands, respectively. The gray areas [1–6] indicate the integration times for which the *RHESSI* spectra in Figure 3 were derived. Bottom: composites of AIA 1600 (red) + 304 (blue) + 131 Å (green) images showing the (E)UV flare emission. The times are indicated on the top panel by letters ((a)–(h)) corresponding to each of the composites. An animation of this figure is available. The video begins at 21:29:56 and ends at 22:14:56. The realtime duration of the animation is 15 s.

(An animation of this figure is available.)

3.2. Soft X-Ray (SXR) Precursors

Flare precursors are enhanced pre-flare SXR emission indicative of small-scale energy release that may play a role in the triggering of the main flare (e.g., van Hoven & Hurford 1984; Veronig et al. 2002; Joshi et al. 2016; Hernandez-Perez et al. 2019). Three precursor episodes (*GOES*–class B7.4, B7.0, and B7.9) were registered by *GOES* and *RHESSI* during the early phase of the M1.3 flare under study (see enhanced 6–12 and 12–25 keV precursor emission highlighted by the yellow and blue areas in the top panel of Figure 2). Each SXR precursor was co-temporal with a localized (E)UV enhancement, occurring at two well-separated locations very compact and low in the corona, i.e., L1 and L2 (see Figures 2(a)–(c) and animation), with a projected distance

of ∼37 Mm. (E)UV observations of the precursors (see P1, P2, and P3 in the insets of Figures 2(a)–(c)) show typical signatures indicative of energy release, i.e., bright loops (indicated by the black dotted lines) connecting chromospheric brightenings (marked by white arrows for P1 and labeled (1,2) for P2 and P3).

The corresponding X-ray imaging and spectroscopy show compact sources that are co-spatial with the precursor sites and weak, yet significant, episodes of enhanced emission (see Figures 3(a)–(c)). Due to low statistics in the X-ray spectra associated with Figure 3(a), a nonthermal component was not included in the fitting. However, at energies >10 keV, a clear enhancement in the photon flux above the thermal fit was registered (marked by a black arrow in Figure 3(a)), indicative
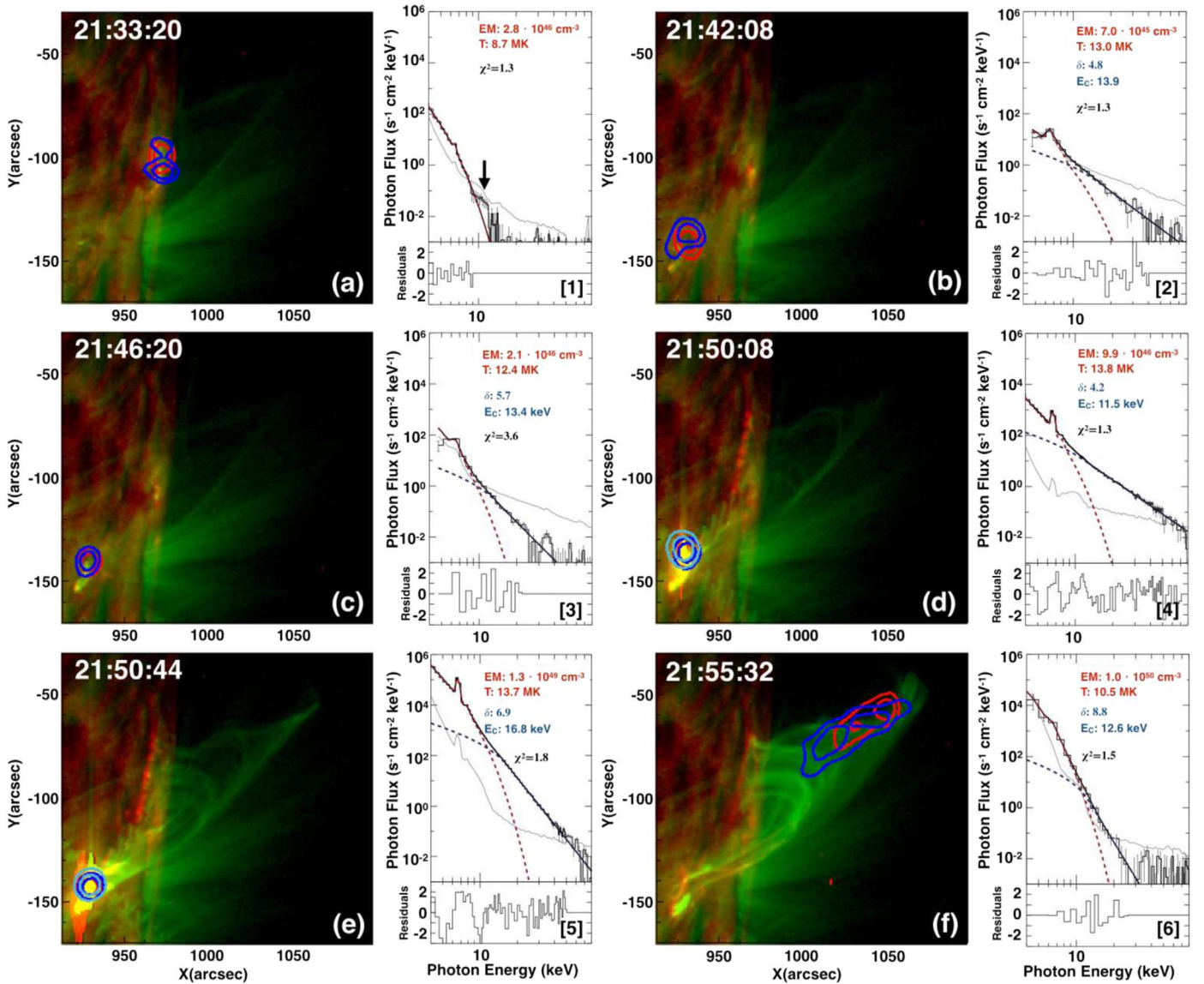
Figure 3. (a)–(f) Composites of AIA 1600 (red) + 131 Å (green) images showing the (E)UV flare emission. The *RHESSI* sources for 3–8 (red), 8–20 (dark blue), and 20–100 keV (light blue) with contours at 60% and 80% of the maximum emission are overplotted. [1–6] corresponding X-ray spectra for the integration times represented by the gray areas in the top panel of Figure 2. All spectra correspond to *RHESSI* with exception of [2] and [3], which show *FERMI* spectra because they provided better statistics. We note that the corresponding *RHESSI* spectra at those times showed very similar results. The X-ray spectra of background-subtracted data (black solid lines) are plotted together with the fitting results for the isothermal component (red dashed lines), and the nonthermal component (blue dashed lines). The background is represented by the gray solid line. The electron temperature, T, emission measure, EM, electron distribution index, δ, and cutoff energy, E_C, as well as the chi-squared of the fitting, χ^2, are listed.

of a weak nonthermal tail. The spectrum associated with P2 and P3 (see Figures 3(b), (c)) showed significant nonthermal emission at these times, co-temporal with an increase in the AIA 94 Å emission during the rest of the early phase (see the AIA 94 Å lightcurve in Figure 2 at 21:42–21:49 UT). The DEM analysis revealed pre-heating episodes at the precursor locations (see Figure 4(a) and animation), accounting for thermal plasma at a temperature of ∼8 MK. The triggering of the flare immediately followed P3.

In order to infer information on the triggering of the event and its magnetic topology, we initially studied the magnetic field of AR 11944 during the flare under study as well as a few days before. We note that due to the rapidly varying photospheric magnetic field of the AR prior to the occurrence of SOL2014-01-13T21:51M1.3, its closeness to the limb, and the small-scale nature of the event, the magnetograms did not

provide us with useful information for the magnetic configuration on the date of the flare occurrence.

3.3. Causal Relationship of Precursors and Flare Features

In addition to the bright loop and associated chromospheric brightenings observed for P2 and P3, the impulsive flare phase starts with the appearance of an additional loop (marked by the orange dashed line in the inset of Figure 2(d)) rooted at a chromospheric brightening (labeled (3)). This was immediately followed by the generation of flare ribbons neighboring L1 and the enhanced emission at L2 as a consequence of nonthermal bremsstrahlung (Figure 2(e)). No X-ray sources were found at the locations where the ribbons formed encompassing L1 (Figures 3(d), (e)), possibly due to *RHESSI*'s limited dynamic range. However, strong nonthermal emission during the impulsive
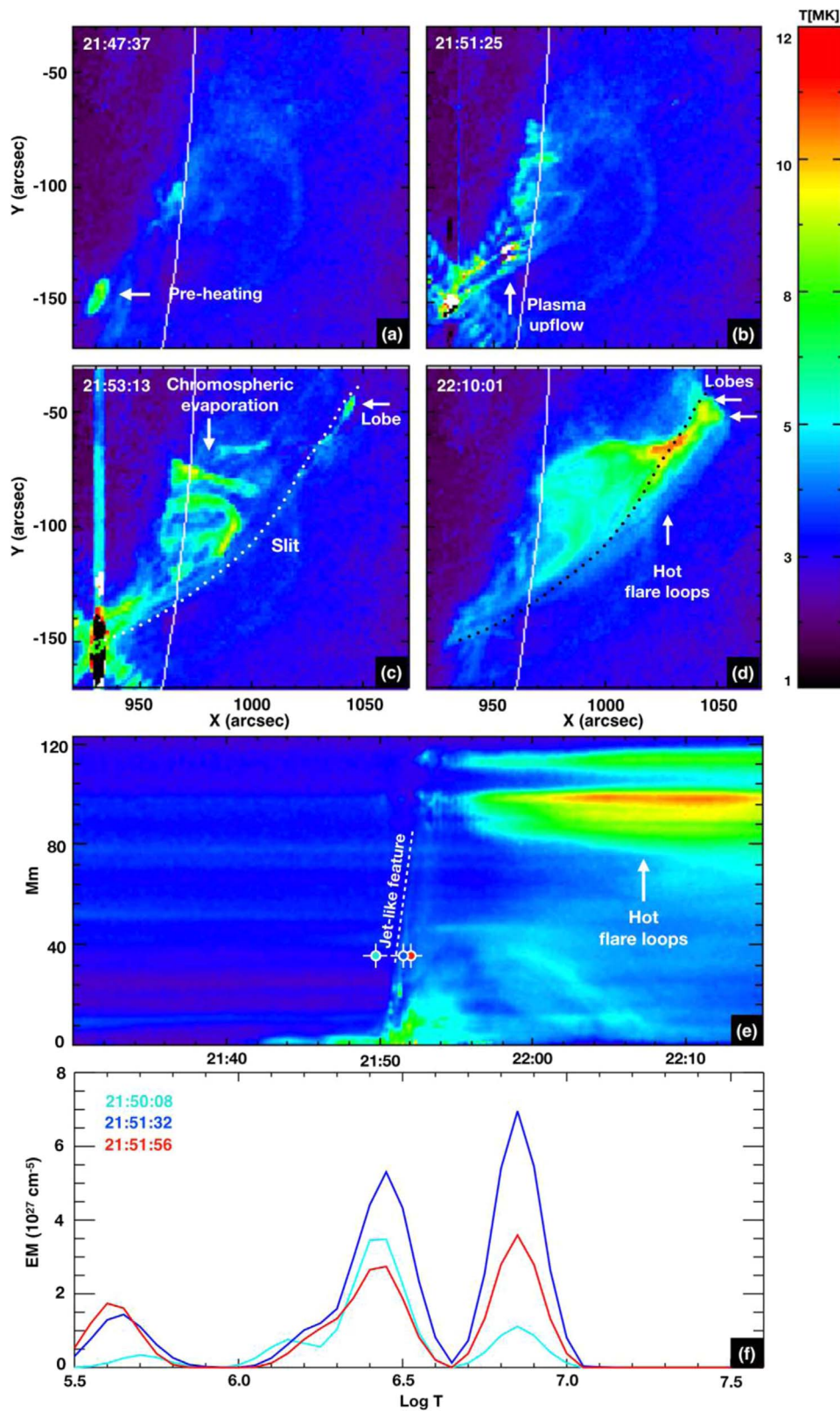
Figure 4. (a)–(d) EM-weighted temperature maps during the M1.3 flare. The dotted lines represent an artificial slit along the trajectory of the jet-like feature, along which we extracted the DEM evolution. (e) Time–distance plot for EM-weighted temperatures along the slit. (f) EM distribution for the position and times marked by the colored circles in panel (e). An animation of panels (a)–(d) is available. The video begins at 21:30:01 and ends at 22:14:49. The realtime duration of the animation is 15 s.

(An animation of this figure is available.)

flare phase was registered at L2, in the form of a compact hard x-ray (HXR) source and a flat nonthermal ($\delta \sim 4.2$) component in the corresponding spectrum (Figure 3(d)). This shows that L2 was the main compact flare region.

During this phase, a jet-like feature emerged from L2 (see inset in Figure 2(e) and Figures 4(d), (e)), reaching its maximum altitude at $[x, y] = [1045'', -45'']$. The EM distribution of a position along the jet-like feature before, during and after its occurrence is shown in Figure 4(f) (see position and corresponding times marked in Figure 4(e)), showing that it was composed of mostly hot plasma above 2 MK, with a major contribution coming from plasma at ~ 6 MK (compare the EM of light and dark blue lines at Log $T = 6.85$). Co-temporal with the jet-like feature reaching its maximum altitude was the occurrence of localized heating (see the white arrow in Figure 4(c)).

3.4. Characteristics of the Cusp-shaped Flare Loops

The impulsive and decay phases revealed the unusual static cusp-shaped appearance of the flare loops, seen in AIA 94 and 131 Å. The loops reach an approximate altitude of 66 Mm above the solar surface, connecting the precursor locations (see Figures 2(e), (f)).

A fast decrease of the SXR emission occurred during the first 6 minutes of the decay phase, i.e., ~ 21:51–21:56 UT (see the red and black lines in Figure 2). The *RHESSI* spectral analysis revealed nonthermal X-ray emission from the high cusp-shaped flare loops (Figure 3(f)). X-ray analysis during the rest of the decay phase was not possible since *RHESSI* entered the Southern Atlantic Anomaly (SAA) and then night time. However, the *GOES* SXR emission did not drop back down to background level. On the contrary, an extended period of enhanced SXR flux followed (above $1.5 \cdot 10^{-6}$ Wm^{-2}), indicative of additional energy release during the decay phase (see the black curve in Figure 2). Similar behavior is exhibited by the AIA 94 Å lightcurve, indicative of further energy input and heating (see green curve in Figure 2). Additionally, enhanced SXR emission in the 6–12 keV energy band in between the SSA and *RHESSI*'s night time is registered. We note that a *RHESSI* image during this period was not possible due to the low number of counts.

(E)UV imaging reveals ongoing heating of the cusp-shaped flare loops while the underlying flare arcade cools down (Figures 2(g), (h)). This led to an unexpected temperature distribution (see Figures 4(d), (f) and animation), i.e., the top of the cusp-shaped flare loops was significantly hotter (~ 10–12 MK) than the arcade underneath (~ 4–6 MK). The temperature of the cusp from the DEM analysis is consistent with the temperature of the thermal plasma derived from the *RHESSI* spectra, of about 10 MK (see the spectrum associated with Figure 3(f)).

4. Discussion and Conclusion

The study of SOL2014-01-13T21:51M1.3 poses challenges to previously reported flare models. Not only was it confined, it exhibited cusp-shaped flare loops, a typical feature of eruptive flares. We studied the early, impulsive, and decay phases in order to understand the initiation and development of such an uncommon structure in confined flares.

(E)UV observations show a direct relationship between the last precursors (P2, P3) and the triggering of the flare, as they were co-spatial and occurred subsequently (Figures 2). HXR

analysis of the precursors revealed the nonthermal nature of P2 and P3 (Figure 3(b), (c)), indicative of accelerated electrons prior to the flare onset (in agreement with e.g., Li et al. 2018a; Hernandez-Perez et al. 2019). This suggests that reconfiguration of the magnetic field due to pre-flare reconnection caused the strong magnetic reconnection and triggered SOL2014-01-13T21:51M1.3 at L2. This is supported by (a) the appearance of an additional bright loop during the early impulsive phase (see the inset of Figure 2(d)) that takes part in the reconnection process, which probably established new connectivity between the lower and higher corona; (b) the strong nonthermal source imaged during the impulsive phase (Figures 3(d), (e)) revealing that L2 is the compact main flare region; and (c) the jet-like feature originating at L2 during the impulsive phase (see the inset in Figure 2(e)).

The triggering of SOL2014-01-13T21:51M1.3 finally exposed its most intriguing observational features: the cusp-shaped appearance of the high-lying flare loops, their prolonged hot emission, and the increasing temperature distribution with height, i.e., all signatures typical of eruptive events (Tsuneta et al. 1992). Given the observational characteristics presented above, the most plausible magnetic scenario is depicted in Figure 5.

We observed a jet-like feature emerging from L2 during the impulsive phase. Jets usually occur due to interchange reconnection (Crooker et al. 2002), e.g., reconnection between closed and open fields that enable the emergence of chromospheric material along the newly reconnected fields (Shibata et al. 1989, 1992; Yokoyama & Shibata 1996). The jet-like feature reported here was most probably generated as a consequence of the reconnection process that established the connectivity between L2 and the higher corona (i.e., reconnection between closed loops of different scales) in a manner similar to interchange reconnection. A simplified sequence depicting this process is represented in Figures 5(b)–(d), showing small loops from L2 (in gray) reconnecting with much larger loops (in green) that establish the connectivity with the higher corona. On the other hand, although the jet-like feature is composed mostly of hot flaring plasma, the low temperature component at transition region temperatures around 0.3–0.5 MK indicates that it could consist of plasma from both the reconnection outflow and chromospheric evaporation from the flare footpoints along the newly reconnected large scale fields (due to the impact of high-energy particles once the connectivity between the lower and higher corona was established). The complex dynamics of chromospheric evaporation flows during flares, microflares, and jets, in particular in transition region lines, has, e.g., been reported in Veronig et al. (2010) and Berkebile-Stoiser et al. (2009).

The heating of the higher corona was initiated by the injection of hot plasma from L2, as suggested by the quick response of the cusp-shaped flare loops during the impulsive phase (Figure 4(e)). The nature of the static high-lying hot flare loops of SOL2014-01-13T21:51M1.3 was clearly different from what has been previously reported in literature (Liu et al. 2014; Gou et al. 2015). The cusp-shaped appearance of the flare loops of SOL2014-01-13T21:51M1.3 (see Figures 2(e)–(h)) is most probably due to a kink of the flare loops (see the green lines in Figure 5). The *RHESSI* sources (of a partly nonthermal nature) near the projected crossing point of the kinked structure during the decay phase (see Figure 3(f)) provide evidence of energy release occurring as a consequence of magnetic reconnection at
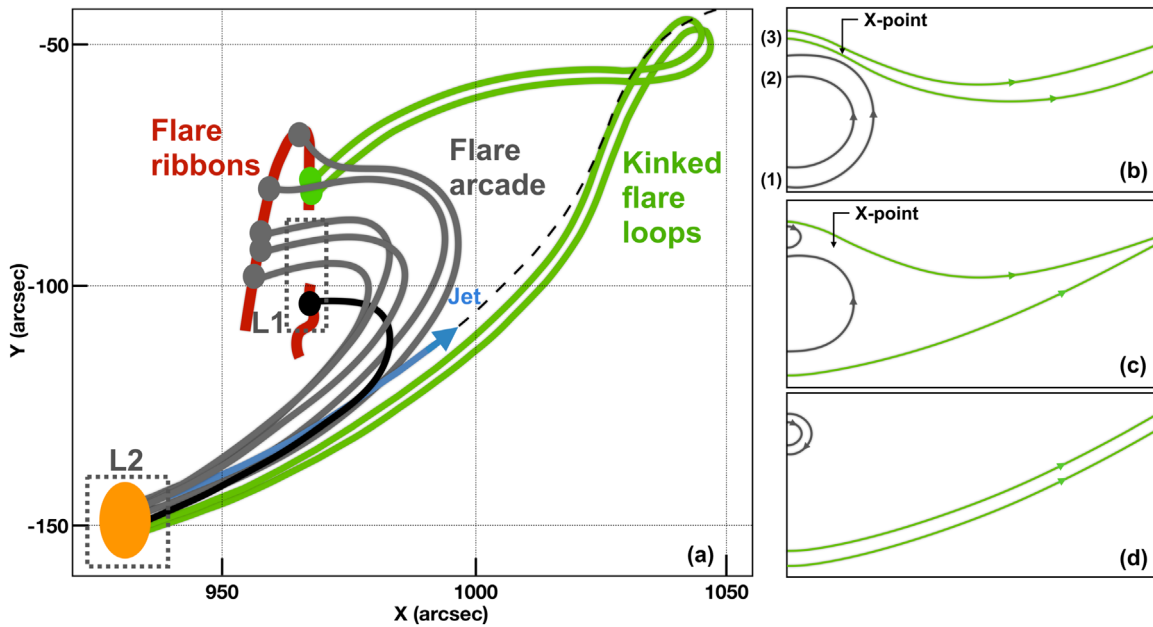
Figure 5. Diagram of the magnetic configuration of the flare. The gray lines represent the flare arcade, the black line is the loop connecting L1 and L2 (see Figure 1(d)). The green lines represent the kinked flare loops. The blue arrow represents the jet-like feature (see Figure 2(e)). Insets [1–3] represent the most probable scenario of interchange reconnection in which the flare was triggered at L2 and the connectivity with the higher corona was established.

the kink. The extended enhanced SXR and EUV emission during the late phase of SOL2014-01-13T21:51M1.3 provides more evidence of a weak process of ongoing energy release (see Figure 2).

X-ray emission at the crossing point of a kinked flux rope as a consequence of magnetic reconnection has been previously imaged in eruptive (e.g., Cho et al. 2009; Liu & Alexander 2009; Guo et al. 2012) and confined events (e.g., Alexander et al. 2006). Whether or not the reconnection event is enough to produce an ejection depends on the degree of twist of the flux rope (e.g., Kliem et al. 2010). However, the nature of the kinked fields in the flare under study differs from the works in the previous studies in that they are not part of a low-lying flux rope but rather enveloping the flare arcade.

We therefore interpret the observed prolonged hot emission and temperature distribution as a consequence of slow magnetic reconnection caused by a strong increase of the thermal pressure at the kink. This can explain the continuous energy release during the late phase revealed by the prolonged SXR emission (see Figure 2), and the increasing temperature distribution with height (see Figure 4(d)). This magnetic configuration also explains why, in this case, we do not observe a growing arcade, a signature of reconnection progressively occurring higher up in the corona, as predicted by the standard flare model.

The answer to an important question remains elusive. Was the kink formed as a consequence of the reconnection at L2, or did it pre-exist before the flare onset? In the first scenario, the flare dynamics initiated by the interchange reconnection at L2 were responsible for the formation of both, the overlying kinked loops as well as the low-lying flare arcade. A possible explanation for the kinked overlying field could involve the transfer of twist in the course of the jet (e.g., Shibata & Uchida 1986). In the second scenario, the overlying field was kinked prior to the flare onset and heated by accelerated particles from L2 and slow magnetic reconnection at the helical current sheet, formed at the interface with the surrounding plasma (e.g., Kliem et al. 2004). The low-lying flare arcade

may then have been produced by reconnection at a current sheet, presumably underlying the kinked structure.

Our study underlines the complexity of flare processes in that features typical of both confined and eruptive flares can be observed in a single event. This must be accounted for by any realistic flare model.

ORCID iDs

Aaron Hernandez-Perez ⓘ https://orcid.org/0000-0003-1201-6950
Yang Su ⓘ https://orcid.org/0000-0002-4241-9921
Julia Thalmann ⓘ https://orcid.org/0000-0001-8985-2549
Astrid M. Veronig ⓘ https://orcid.org/0000-0003-2073-002X
Karin Dissauer ⓘ https://orcid.org/0000-0001-5661-9759
Bhuwan Joshi ⓘ https://orcid.org/0000-0001-5042-2170
Ramesh Chandra ⓘ https://orcid.org/0000-0002-3518-5856

References

Alexander, D., Liu, R., & Gilbert, H. R. 2006, ApJ, 653, 719
Benz, A. O. 2017, LRSP, 14, 2
Berkebile-Stoiser, S., Gömöry, P., Veronig, A. M., Rybák, J., & Sütterlin, P. 2009, A&A, 505, 811
Brown, J. C. 1971, SoPh, 18, 489
Carmichael, H. 1964, NASSP, 50, 451
Chen, X., Yan, Y., Tan, B., et al. 2019, ApJ, 878, 78
Cheung, M. C. M., Boerner, P., Schrijver, C. J., et al. 2015, ApJ, 807, 143
Cho, K.-S., Lee, J., Bong, S.-C., et al. 2009, ApJ, 703, 1
Crooker, N. U., Gosling, J. T., & Kahler, S. W. 2002, JGRA, 107, 1028
Forbes, T. G. 2000, JGR, 105, 23153
Glesener, L., Krucker, S., Hannah, I. G., et al. 2017, ApJ, 845, 122
Gou, T., Liu, R., & Wang, Y. 2015, SoPh, 290, 2211
Guo, Y., Ding, M. D., Schmieder, B., Démoulin, P., & Li, H. 2012, ApJ, 746, 17
Hernandez-Perez, A., Su, Y., Veronig, A. M., et al. 2019, ApJ, 874, 122
Hernandez-Perez, A., Thalmann, J. K., Veronig, A. M., et al. 2017, ApJ, 847, 124
Heyvaerts, J., Priest, E. R., & Rust, D. M. 1977, ApJ, 216, 123
Hirayama, T. 1974, SoPh, 34, 323
Holman, G. D., Sui, L., Schwartz, R. A., & Emslie, A. G. 2003, ApJL, 595, L97
Hou, Y., Li, T., Yang, S., & Zhang, J. 2019, ApJ, 871, 4
Hurford, G. J., Schmahl, E. J., Schwartz, R. A., et al. 2002, SoPh, 210, 61
Joshi, B., Kushwaha, U., Veronig, A. M., & Cho, K.-S. 2016, ApJ, 832, 130
Joshi, N. C., Liu, C., Sun, X., et al. 2015, ApJ, 812, 50
Kliem, B., Linton, M. G., Török, T., & Karlický, M. 2010, SoPh, 266, 91
Kliem, B., Titov, V. S., & Török, T. 2004, A&A, 413, L23
Kopp, R. A., & Pneuman, G. W. 1976, SoPh, 50, 85
Lemen, J. R., Title, A. M., Akin, D. J., et al. 2012, SoPh, 275, 17
Li, D., Li, Y., Su, W., Huang, Y., & Ning, Z. 2018a, ApJ, 854, 26
Li, T., Yang, S., Zhang, Q., Hou, Y., & Zhang, J. 2018b, ApJ, 859, 122
Lin, R. P., Dennis, B. R., Hurford, G. J., et al. 2002, SoPh, 210, 3
Liu, R., & Alexander, D. 2009, ApJ, 697, 999
Liu, R., Titov, V. S., Gou, T., et al. 2014, ApJ, 790, 8
Masson, S., Pariat, E., Aulanier, G., & Schrijver, C. J. 2009, ApJ, 700, 559
Meegan, C., Lichti, G., Bhat, P. N., et al. 2009, ApJ, 702, 791
Melrose, D. B. 1997, ApJ, 486, 521
Pesnell, W. D., Thompson, B. J., & Chamberlin, P. C. 2012, SoPh, 275, 3
Reid, H. A. S., Vilmer, N., Aulanier, G., & Pariat, E. 2012, A&A, 547, A52
Shibata, K., Nozawa, S., & Matsumoto, R. 1992, PASJ, 44, 265
Shibata, K., Tajima, T., Steinolfson, R. S., & Matsumoto, R. 1989, ApJ, 345, 584
Shibata, K., & Uchida, Y. 1986, SoPh, 103, 299
Sturrock, P. A. 1966, Natur, 211, 697
Su, Y., Veronig, A. M., Hannah, I. G., et al. 2018, ApJL, 856, L17
Tsuneta, S. 1996, ApJ, 464, 1055
Tsuneta, S., Hara, H., Shimizu, T., et al. 1992, PASJ, 44, L63
van Hoven, G., & Hurford, G. J. 1984, AdSpR, 4, 95
Veronig, A., Vršnak, B., Temmer, M., & Hanslmeier, A. 2002, SoPh, 208, 297
Veronig, A. M., Karlický, M., Vršnak, B., et al. 2006, A&A, 446, 675
Veronig, A. M., & Polanec, W. 2015, SoPh, 290, 2923
Veronig, A. M., Rybák, J., Gömöry, P., et al. 2010, ApJ, 719, 655
Yokoyama, T., & Shibata, K. 1996, PASJ, 48, 353
Yurchyshyn, V. B., Wang, H., Qiu, J., Goode, P. R., & Abramenko, V. I. 2000, ApJ, 540, 1143
Zhang, Q. M., Cheng, J. X., Feng, L., et al. 2019, ApJ, 883, 124
Zhong, Z., Guo, Y., Ding, M. D., Fang, C., & Hao, Q. 2019, ApJ, 871, 105